Computational Model for Amoeboid Motion: Coupling Membrane and Cytosol Dynamics

Adrian Moure* and Hector Gomez

Universidade da Coruña, Campus de Elviña, 15071, A Coruña, Spain

(Dated: October 26, 2016)

Abstract

A distinguishing feature of amoeboid motion is that the migrating cell undergoes large deformations, caused by the emergence and retraction of actin-rich protrusions, called *pseudopods*. Here, we propose a cell motility model that represents pseudopod dynamics, as well as its interaction with membrane signaling molecules. The model accounts for internal and external forces, such as protrusion, contraction, adhesion, surface tension, or those arising from cell-obstacle contacts. By coupling the membrane and cytosol interactions we are able to reproduce a realistic picture of amoeboid motion. The model results are in quantitative agreement with experiments and show how cells may take advantage of the geometry of their microenvironment to migrate more efficiently.

PACS numbers: 87.17.Jj, 87.17.Aa, 87.17.Rt

* a.moure.rosende@udc.es

I. INTRODUCTION

A fascinating feature of eukaryotic cells is their ability to move. Cellular motility controls crucial biological processes, for example, cellular nourishment, wound healing, tissue growth, pathogen removal, or metastatic disease [1, 2]. Cell migration through biological tissues is an exceedingly complex process, which is usually understood as a continuous cycle of five interdependent steps, namely, (1) protrusion and elongation of the leading edge driven by actin polymerization; (2) cell-matrix interaction and formation of focal contacts via transmembrane adhesion proteins; (3) extracellular matrix degradation by cell surface proteases; (4) actomyosin contraction generated by active myosin II bound to actin filaments; and (5) detachment of the trailing edge and slow glide forward [3].

This paper deals with pseudopodial amoeboid motion of a single cell, a mode of migration where locomotion is achieved by rapidly protruding and retracting extensions generally called *pseudopods.* This kind of motion is often studied using simplified systems such as the planar movement of *Dictyostelium discoideum. Dictyostelium* is an elongated and extraordinarily deformable cell that translocates via rapidly alternating cycles of morphological expansion and contraction [see Fig. 1(a)]. These cells produce dynamic actin-rich protrusions at their leading edge, the aforementioned pseudopods, which locally drive the edge of the cell outwards. Our philosophy follows the so-called *pseudopod-centered view*, in which external signals are not necessary for pseudopod formation [4]. The motion of *Dictyostelium* is the result of an ordered sequence of expansion and retraction steps. Each expansion step corresponds to the formation of a new pseudopod, which may occur by splitting an existing protrusion or by generating one *de novo* [5] [see Fig. 1(a)]. The way in which the growth of new pseudopods is orchestrated leads to the so-called persistent motion. Persistence is the cell's tendency to keep moving in the same direction for a period of time [6]. Classical experiments [6, 7] show that persistent cells are able to colonize farther environments than cells that move in uncorrelated directions (random motion without persistence). This could have implications in many biological processes.

Computational modeling of cell motility has advanced significantly over the last few years [8, 9]. There has been abundant work modeling the membrane mechanics and its signaling activity [10–13]. There are also models that describe in detail the cytosol dynamics [14–16], though most of them have focused on mesenchymal motility, in which cells extend
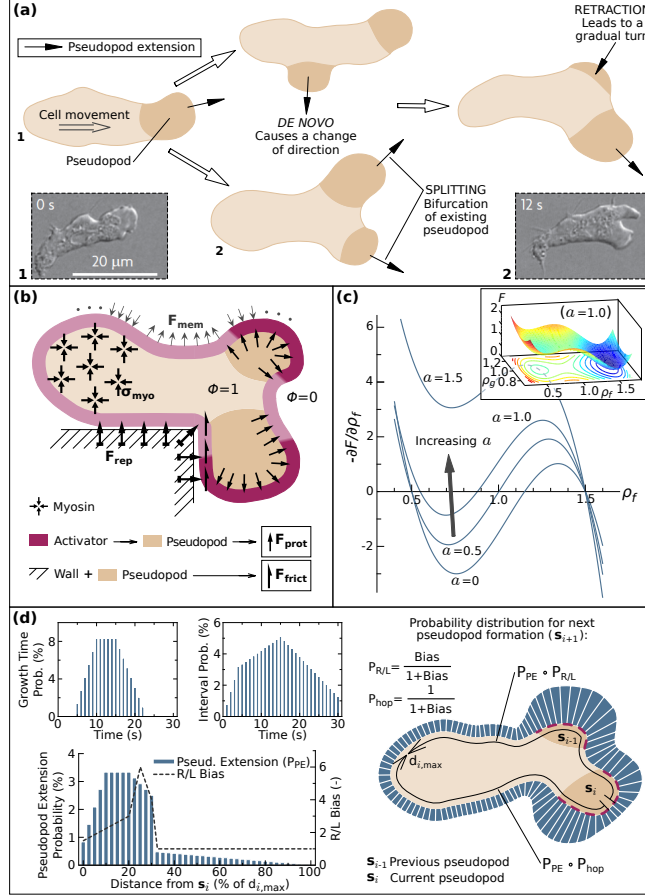
FIG. 1. (Color online) Conceptual and computational model for amoeboid motion. (a) Expansion and retraction of pseudopods. The dashed rectangles show experimental images taken from [4]. (b) Computational model for amoeboid motion. (c) Derivative of the function F with respect to F-actin concentration, depending on the activator concentration. The inset shows the function F for $a=1$. (d) Probability distributions for growth time, interval, and location of pseudopods, derived from [5].

a stationary lamellipodium at the leading edge. However, coupled models including the cytosolic machinery and membrane dynamics have received little attention, even though they are critical to understand cell migration [17]. Here, we show that modeling the *coupled* interaction of the membrane signaling activity and the cytosol dynamics allows to understand the mechanisms that control pseudopod formation and, thus, amoeboid motion. Our theory predicts realistic myosin and actin distributions within the cell and reproduces experimental laws of spreading. The coupled model allows to study how external forces exerted on the membrane (e.g., those caused by rigid obstacles) modify the cytosol dynamics. Our model

also explains how cells may exploit particular geometric features of their environment to find more efficient migration strategies.

II. THE MODEL

We use a phase-field $\phi(\boldsymbol{x}, t)$ to track the cell's location. The cytosolic machinery is described by three fields, namely, $\rho_f(\boldsymbol{x}, t)$, $\rho_g(\boldsymbol{x}, t)$, and $\rho_m(\boldsymbol{x}, t)$, that represent the density of actin filaments (F-actin), globular actin subunits (G-actin), and molecular motors myosin II, respectively. We simplify the membrane signaling dynamics by using a single membrane-located activator $a(\boldsymbol{x}, t)$ that triggers the growth of new pseudopods. In our model, pseudopods push the membrane outwards and are localized regions of F-actin in the form of protrusive structures. Myosin, in contrast, produces contractile forces in the cell rear [see Fig. 1(b)]. The actin filament network is treated as a viscous fluid [15], whose velocity $\boldsymbol{u}(\boldsymbol{x}, t)$ is governed by a Stokes-type equation [18]. Full details of our model and the parameter values used in the simulations may be found in Appendix A.

Cell motion. The cell's position is given by the phase field ϕ, which transitions smoothly from 0 (outside the cell) to 1 (inside the cell). The cell's membrane is defined by the level set $\phi = 1/2$ and moves driven by the velocity of the actin network $\boldsymbol{u}$. The evolution equation for ϕ is

$$\frac{\partial \phi}{\partial t} + \boldsymbol{u} \cdot \nabla \phi = R, \tag{1}$$

where $R = \Gamma \left(\varepsilon \nabla^2 \phi - G'(\phi)/\varepsilon + c\varepsilon |\nabla \phi| \right)$ [19]. Here, $\varepsilon > 0$ is a small constant and $R \sim \varepsilon$ maintains a hyperbolic tangent profile between $\phi = 0$ and $\phi = 1$. The constant $\Gamma > 0$ sets the strength of the R, while $c = -\nabla \cdot (\nabla \phi/|\nabla \phi|)$ denotes the curvature of the membrane, and $G(\phi) = 18\phi^2(1-\phi)^2$ is a double-well potential with minima at $\phi = 0$ and $\phi = 1$ [14, 15]. Eq. (1) may be also thought of as a stabilized level set equation.

Myosin dynamics. We assume that myosin is transported by the actin network velocity and diffuses throughout the cell. Since the cell's position changes with time, the classical approach would be to solve an equation on a moving domain. By using the phase-field method, we can solve (on a fixed domain) the equivalent equation

$$\frac{\partial (\phi \rho_m)}{\partial t} + \nabla \cdot (\phi \rho_m \boldsymbol{u}) = \nabla \cdot [D_m(\rho_f)\phi \nabla \rho_m]. \tag{2}$$

The key idea is to introduce the cell's position marker ϕ in the time derivative, as well as in

the convection and diffusion operators [20]. In Eq. (2), the function $D_m(\rho_f) = D_{\max}/(1 + K^2\rho_f^2)$, where $D_{\max}$ and K are constants, produces an effective advection that transports myosin away from protruding F-actin regions, thereby concentrating myosin to the cell's rear and provoking contraction of the back end of the cell.

Activator dynamics. The growth of pseudopods is controlled by membrane signaling molecules that trigger actin nucleation, for example, PIP3 [21]. In our model, this is represented by the concentration of a generic substance that we call activator. We make use again of the phase-field method to localize the activator dynamics to the membrane without resorting to surface partial differential equations. We propose the equation

$$\frac{\partial(\delta_m a)}{\partial t} + \nabla \cdot (\delta_m a \boldsymbol{u}) = \nabla \cdot (D_a \delta_m \nabla a)$$
$$-r_a \delta_m a + b_a \delta_m S_a, \tag{3}$$

where $\delta_m = \exp[-\varphi(\phi - 0.5)^2]$ is a smooth marker of the membrane and the parameter φ defines its thickness. In Eq. (3), D_a is the diffusion constant, r_a is the rate of natural decay, and $S_a = (a_{max} - a)\sum_i \delta_{\boldsymbol{x},i}\delta_{t,i}$ is a source term that drives a to a_{max} at certain time intervals and spatial points of the membrane, at a rate controlled by the parameter b_a. The peaks of activator concentration produced by S_a will trigger the growth of new pseudopods. Each peak is associated to an integer index i, such that the function $\delta_{t,i}$ localizes the growth of new peaks to a certain periods of time, and its spatial location is given by the function $\delta_{\boldsymbol{x},i}$, which is non-zero in a small area of the membrane. To establish the spatial location of a new peak [$\boldsymbol{s}_{i+1}$ in Fig. 1(d)], we resort to the probability distribution plotted in Fig. 1(d), which depends on the position of the two previous peaks ($\boldsymbol{s}_{i-1}$ and $\boldsymbol{s}_i$). According to Fig. 1(d), the probability function will be $P_{PE} \cdot P_{R/L}$ on the side of the membrane where $\boldsymbol{s}_{i-1}$ is placed, and $P_{PE} \cdot P_{hop}$ on the other side (this bias is a consequence of persistent motion). Once a peak emerges, the next one will arise after the end of the *interval* time, and each peak will be active during the *growth time*. Since the interval and the growth time are two different random variables, whose distributions are given in Fig. 1(d), there may be none, one, or more than one active peaks at the same time. All probability functions shown in Fig. 1(d) have been derived from experimental data [5]. More details about $\delta_{t,i}$ and $\delta_{\boldsymbol{x},i}$ can be found in Appendix A.

Actin dynamics. Actin undergoes phase transformations by alternating between a globular (G-actin) and a filamentous (F-actin) state. In addition, F-actin may be in the form

5

of a protrusive or a passive structure. Protrusive structures are identified with pseudopods and their growth is triggered by the activator. We make use of the phase-field theory [22] to propose a new model of actin dynamics based on the free energy functional

$$
\mathcal{F}[\rho_f, \rho_g] = \int_\Omega \phi \left[\frac{\varepsilon_f^2}{2} |\nabla \rho_f|^2 + \frac{\varepsilon_g^2}{2} |\nabla \rho_g|^2 + F(\rho_f, \rho_g, a) \right] d\Omega
$$
$$
+ \frac{\alpha}{2} \left(\mathcal{N}_0 - \mathcal{N}[\rho_f, \rho_g] \right)^2, \tag{4}
$$

where $\mathcal{N}[\rho_f, \rho_g] = \int_\Omega \phi(\rho_f + \rho_g) d\Omega$ represents the amount of actin within the cell and $\mathcal{N}_0$ is the value of $\mathcal{N}$ at the initial time. Thus, the last term in Eq. (4) is a penalty term that keeps $\mathcal{N}$ constant in time, where α determines its strength. The parameters ε_f and ε_g represent diffusive length scales of ρ_f and ρ_g, respectively. The function F controls the phase transitions in terms of the activator concentration, and can be expressed as

$$
F(\rho_f, \rho_g, a) = 10(\rho_f - 1.5)^2(\rho_f - 0.5)^2 + 7.5(\rho_g - 1.0)^2 +
$$
$$
I(a)(\rho_f - 1.5)^2[\rho_f + \beta(a)I(a)], \tag{5}
$$

where $I(a) = a^2 - 2\exp(-4a)$ and $\beta(a) = 0.5[1 - (a - 1.8)^2/1.8^2]$. F is a convex function of ρ_g with a unique minimum at $\rho_g = 1$, which represents the stable density of G-actin. However, F may be a convex or non-convex function of ρ_f depending on the value of a. When a is small, F is a double well potential [see Fig. 1(c), inset]. The wells correspond to two stable densities of F-actin, one associated to protrusive structures (higher density, $\rho_f = 1.5$) and another to passive networks (lower density, $\rho_f \approx 0.5$). Within the range of small values of a, the well representing protrusive structures is energetically favored for larger values of a [e.g., case $a = 1.0$ in Fig. 1(c)]. The opposite happens for smaller values of a [see Fig. 1(c), case $a = 0$]. If a is sufficiently large [e.g., case $a = 1.5$ in Fig. 1(c)], F becomes a convex function with only one local minimum associated to protrusive structures. Using the free energy functional in Eq. (4), we can utilize the framework of classical non-conserved dynamics to derive the evolution equations

$$
\frac{\partial(\phi\rho_f)}{\partial t} + \nabla \cdot (\phi\rho_f \boldsymbol{u}) = -\Gamma_f \frac{\delta \mathcal{F}}{\delta \rho_f} \tag{6}
$$
$$
\frac{\partial(\phi\rho_g)}{\partial t} + \nabla \cdot (\phi\rho_g \boldsymbol{u}) = -\Gamma_g \frac{\delta \mathcal{F}}{\delta \rho_g} \tag{7}
$$

where Γ_f and Γ_g are constants, and $\delta\mathcal{F}/\delta\rho_f$ and $\delta\mathcal{F}/\delta\rho_g$ are the variational derivatives of the energy with respect to F-actin and G-actin concentration, respectively, which may be

written as

$$\frac{\delta \mathcal{F}}{\delta \rho_f} = -\varepsilon_f^2 \nabla \cdot (\phi \nabla \rho_f) + \phi \frac{\partial F}{\partial \rho_f} + \alpha \phi (\mathcal{N} - \mathcal{N}_0), \tag{8}$$

$$\frac{\delta \mathcal{F}}{\delta \rho_g} = -\varepsilon_g^2 \nabla \cdot (\phi \nabla \rho_g) + \phi \frac{\partial F}{\partial \rho_g} + \alpha \phi (\mathcal{N} - \mathcal{N}_0). \tag{9}$$

Actin flow. The actin filament network is treated as a viscous flow governed by a Stokes-type equation augmented with forces specific to amoeboid motion. We propose the equation

$$\nabla \cdot (\boldsymbol{\sigma} + \boldsymbol{\sigma}_{myo} + \boldsymbol{\sigma}_{prot}) + \boldsymbol{F}_{adh} + \boldsymbol{F}_{mem} + \boldsymbol{F}_{wall} = 0, \tag{10}$$

where $\boldsymbol{\sigma} = \phi[\mu(\nabla \boldsymbol{u} + \nabla \boldsymbol{u}^T) + \lambda \nabla \cdot \boldsymbol{u}\boldsymbol{I}]$ is the classical stress tensor of a Newtonian fluid localized to the cell's interior. Here, μ and λ are the viscosity coefficients, and $\boldsymbol{I}$ is the identity tensor. The isotropic contractile stress generated by myosin is given by $\boldsymbol{\sigma}_{myo} = \phi \rho_m \eta_m(\rho_m)\boldsymbol{I}$, where $\eta_m(\rho_m)$ is a function producing greater stress where myosin concentration is higher. The stress caused by F-actin protrusions is normal to the membrane and takes the form $\boldsymbol{\sigma}_{prot} = -\phi \rho_f \eta_f(\rho_f) \delta_f \nabla \phi \otimes \nabla \phi$. The quantity δ_f is simply a marker of the location of rigid obstacles that annihilates $\boldsymbol{\sigma}_{prot}$ in the vicinity of barriers, and $\eta_f(\rho_f)$ controls the protrusive stress such that it can only arise at areas with high density of F-actin. The adhesion force $\boldsymbol{F}_{adh} = -\varsigma \boldsymbol{u}$ represents a continuous drag force proportional to filament velocity, with ς being the friction coefficient. $\boldsymbol{F}_{mem}$ accounts for the forces exerted by the cell's membrane. We neglect bending forces [23] and consider only the force induced by surface tension. This force is proportional to the membrane's curvature and is oriented in the direction orthogonal to the membrane. Using the phase-field theory, surface tension forces can be expressed as $\boldsymbol{F}_{mem} = -\gamma(\varepsilon \nabla^2 \phi - G'(\phi)/\varepsilon)\nabla \phi$, where γ is the surface tension coefficient. Finally, $\boldsymbol{F}_{wall}$ represents the contact forces exerted on the cell by a rigid obstacle. We express this force as $\boldsymbol{F}_{wall} = \boldsymbol{F}_{rep} + \boldsymbol{F}_{fr}$, where $\boldsymbol{F}_{rep}$ and $\boldsymbol{F}_{fr}$ are, respectively, repulsion and friction forces [24, 25]. Repulsion forces are orthogonal to the solid obstacle, while friction forces are tangential. Repulsive forces may be expressed as $\boldsymbol{F}_{rep} = \nabla \cdot \boldsymbol{\sigma}_{rep}$, where $\boldsymbol{\sigma}_{rep} = \phi \eta_{rep} \delta_{wall}^{rep} \nabla \phi \otimes \nabla \phi$. The parameter η_{rep} controls the strength of repulsive forces, the smooth function δ_{wall}^{rep} localizes these forces to the vicinity of the wall, and the term $\nabla \phi \otimes \nabla \phi$ naturally makes them vanish away from the membrane. Friction forces may be modeled as $\boldsymbol{F}_{fr} = -\varsigma_{fr} \delta_{fr} \boldsymbol{t}$, where $\boldsymbol{t}$ is the unit tangent vector to the wall pointing in the direction of the cell's velocity. $\boldsymbol{F}_{fr}$ is non-zero only when a pseudopod is pushing the wall [26], which is accomplished with the localizer δ_{fr} (see Appendix A). ς_{fr} is a function of the cell velocity

7

given by $\varsigma_{fr}(\boldsymbol{u}_{cell}) = \varsigma_{fr}^{M}[1 - \exp(-K_u\boldsymbol{u}_{cell})]$ [27, 28], where ς_{fr}^{M} and K_u are constants, and $\boldsymbol{u}_{cell}$ is the velocity of the center of mass of the cell. More details of our model may be found in Appendix A.

Our model presents several differences and advantages in comparison with other models. The first one is the description of the actin dynamics through the functional $\mathcal{F}$. Here, the actin behavior is similar to the wave-pinning model [15, 29], but including a dependence on the activator. Since we introduce this dependence in the energy functional, the relationship between actin and the activator in the evolution equations follows directly from our variational derivation. Most amoeboid motility models have focused on the membrane dynamics [10, 11] and have simulated the cell as an evolving surface [12, 13] resorting to surface PDEs, a moving mesh, and even employing more than one mesh [30]. Most of them do not account for cytosolic components explicitly. However, our model considers both membrane and cytosolic compounds by using a single fixed mesh, thanks to the phase-field framework. Other feature of our model is the cell-obstacle interaction that we simply introduce through the force $\boldsymbol{F}_{wall}$. Previous approaches to do this include the introduction of a repulsive potential [31], but this complicates the coupling with other components of the model. Other authors have imposed a vanishing velocity condition on the nodes where the cell is in contact with the obstacle [32], but this introduces a discrete component in the model and our goal was to derive a continuous model. Finally, the coupling between the cytosol and the membrane allows to represent different behaviors of the intracellular compounds that can not be captured by uncoupled models. As we will show in following sections, when the cell is subjected to compressive forces (e.g., those exerted by the walls of a narrow channel) the F-actin network extends over the entire cytosol rather than over localized areas. The coupling is essential to capture this process.

From a computational point of view, we have to solve Eqs. (1)–(3),(6),(7), and (10) on a single fixed mesh. We consider a two-dimensional system and use Isogeometric Analysis [33], a spline-based finite element method that features higher-order accuracy and robustness in nonlinear problems. We use quadratic square elements of size $0.2\,\mu m$ and a time step of 0.05 s. Further refinement did not produce noticeable changes in the solutions.
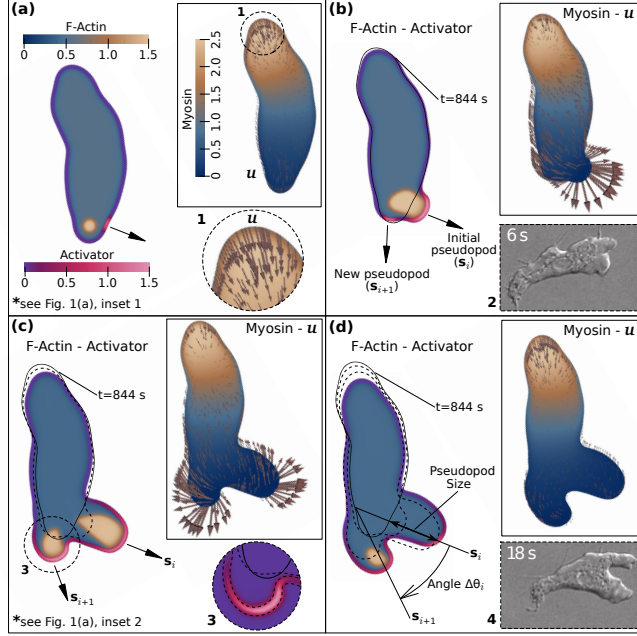
FIG. 2. (Color online) Free movement snapshots. F-actin and activator distributions at $t = 844$, 847, 852, and 857 s (myosin and velocity distributions are represented inside boxes). Insets 2 and 4 show experimental images taken from [4]; see insets 1 and 2 in Fig. 1(a) for completeness. (a) $t = 844$ s. The velocity distribution is zoomed in. (b) $t = 847$ s. (c) $t = 852$ s. The activator distribution is zoomed in. (d) $t = 857$ s. Description of pseudopod size and angle between pseudopods.

III.   FREE MOVEMENT RESULTS

We initially focus on the free movement of *Dictyostelium* on a planar surface. We performed 10 independent simulations, each corresponding to the motion of one cell for 15 minutes. The initial condition defines a circular cell of radius 8 µm with no activator on the membrane, uniform ρ_f, ρ_g, and ρ_m densities, zero velocity, and a random location for the first pseudopod. We first focus on small-scale features of the model, such as the cytosol or activator dynamics within the cell. Figure 2 shows the cell shape at four different times: 844, 847, 852, and 857 s (solid and dashed black lines in the main panels indicate the cell's membrane position at previous times). We represent the F-actin distribution within the cell and the activator concentration on the membrane, as well as the velocity and myosin distribution inside boxes. At $t = 844$ s, a new activator peak has just appeared and triggers the formation of a new pseudopod (let us call it $\boldsymbol{s}_i$), which will grow until $t = 857$ s. At that time, the pseudopod is no longer extending, but beginning its retraction. At $t = 847$ s, near the

initial pseudopod, there is a crescent activator peak that will cause the formation of a new pseudopod ($\boldsymbol{s}_{i+1}$) by splitting the current one few seconds later [see Figs. 2(c)-(d)]. We can observe that myosin is concentrated at the rear of the cell, producing the retraction of the membrane [see Fig. 2(a), zoom 1], and the F-actin velocity is able to reproduce retrograde flow in regions of growing lamellipodia. Finally, we compare experimental images taken from [4] to our results [see Fig. 1 (insets 1 and 2) and Fig. 2 (insets 2 and 4)], and we conclude that qualitative features such as cell shape, F-actin distribution, or the general dynamic behavior exhibit great similarities. The videos in [34] show a highly-dynamic motion with striking resemblance to experiments of amoeboid movement.

Figures 3(a)-(b) illustrate how our model reproduces larger-scale features and emerging behavior, such as persistent motion. Figure 3(a) shows the predicted tracks of 10 cells compared with experimental results (see the inset). The cells tracks seem to maintain their direction for certain periods of time, suggesting persistent motion. For a more detailed quantitative comparison, we make use of the *mean squared displacement* (MSD) [6, 7], a widely used measure of the spatial extent of random motion. More specifically, $\mathrm{MSD}(t) = (\sum_{i=1}^{n_c} |\boldsymbol{x}_i(t) - \boldsymbol{x}_i(0)|^2)/n_c$, where n_c is the number of cells and $\boldsymbol{x}_i(t)$ is the position of the cell's centroid at time t. As shown in Fig. 3(b), the time evolution of the MSD exhibits a quasi-quadratic behavior for early times and a linear growth for late times, as expected for persistent motion. The plot shows quantitative agreement with the experiment [5]. Following the quantitative analysis, the pseudopod size and the angle between consecutive pseudopods have been measured according to description in Fig. 2(d), and have been plotted in Fig. 3(c), left. The results are quite similar to experimental data [5, 35] (note that we have not distinguished between splitting or *de novo* pseudopods) and to other *Dictyostelium* motility models results [13, 30]. This resemblance could seem redundant, since we have introduced the pseudopod formation probability in the model, but it should be noticed that only the initial location of the activator patch is given. Though the correlation between the activator and pseudopod locations is high (as observed in [13]), the pseudopod growth is led by the actin dynamics. Therefore, the shape, size, and angle between pseudopods naturally arise in our model. We have also plotted the angle between three consecutive pseudopods in Fig. 3(c), middle top. Here, the top-left and the bottom-right quadrants are denser than the two others, a typical feature of persistent motion [5, 35] (the most frequent sequence is a turn left after a turn right, and vice versa). We have finally analyzed the cell's instant
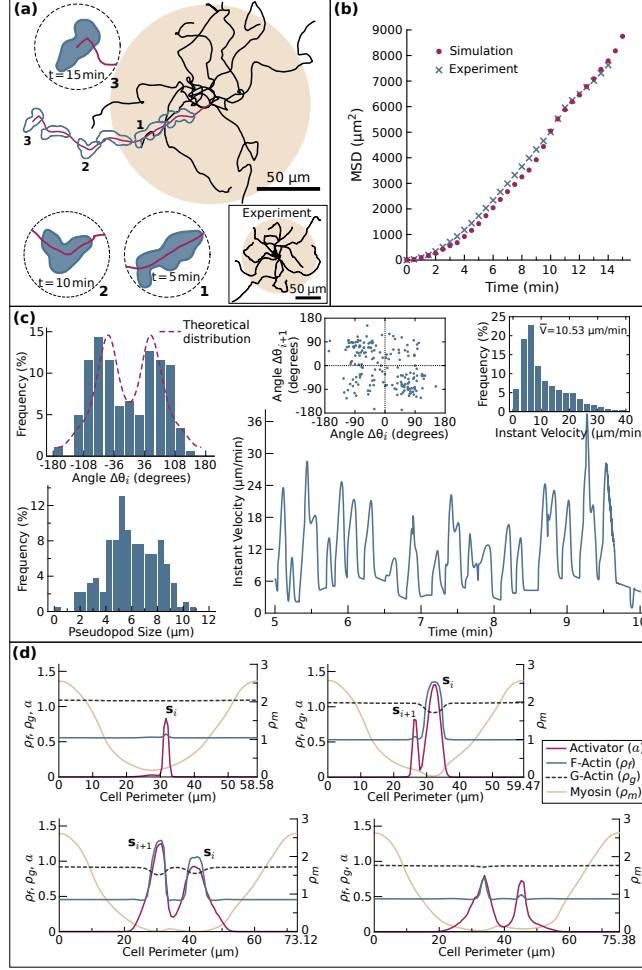
FIG. 3. (Color online) Free movement results analysis. (a) Comparison of cells tracks with experiment [5]. Some snapshots of the cell shape corresponding to the red track are zoomed in. (b) Comparison of the computational Mean Squared Displacement with experiment [5]. (c) Histograms of: pseudopod size, angle between two correlative pseudopods, and instant velocity. $\Delta\theta_i$ angle plotted against $\Delta\theta_{i+1}$ angle. Temporal evolution of instant velocity. (d) Activator, F-actin, G-actin and myosin distributions along the cell membrane corresponding to the snapshots shown in Fig. 2 (from left to right and top to bottom, $t = 844, 847, 852,$ and 857 s).

velocity. The average (over time and cell population) takes the value $\bar{V} = 10.53\,\mu\text{m/min}$ in the simulations and $10.4\,\mu\text{m/min}$ in the experiment [5]. A histogram and a 5 minute-long graph with the temporal evolution of the instant velocity can be found in Fig. 3(c), right. Both of them display great similarities to their respective plots in [35, 36], showing the presence of fluctuations around the average velocity, on the time-scale of minutes. In the

11

temporal plot, each peak corresponds to the extension of a pseudopod, causing also peaks in the cell's area and perimeter plots (not shown). Figure 3(d) shows the temporal evolution of the main variables along the membrane, corresponding to the snapshots plotted in Fig. 2. The aforementioned relationship between F-actin and activator can be observed, as well as the decrease of myosin II in areas of pseudopod extension. Note the growth of the membrane and the fluctuation of G-actin around values of 1.0, depending on the global state of the cell and the location of high density patches of F-actin.

IV.   CONFINED MOVEMENT RESULTS

Let us now focus on confined movement. We compare our model results with the experiments in [36, 37], which study cell motility in microchannels [see Figs. 4(b), bottom and 4(d)]. The experiments analyze how the microchannel width modifies the ability of cells to spread. In narrow channels, wall friction slows down the cell, whereas in wider channels the cell is unable to contact both sides, reducing its forward protrusion [24] and acquiring a more random phenotype. There seems to be an optimal channel width that maximizes spreading.

To get representative results, we performed 8 simulations of 15 minutes for each channel width (6, 8, 10, 12, 14, and 16 μm). Figures 4(a)–(c) show several snapshots of F-actin, activator, velocity and myosin distributions for widths of 6, 10, and 16 μm (cell's membrane positions at previous times are displayed with black lines), which can be compared with the experiments in Figs. 4(b), bottom and 4(d). In the case of narrow channels, the F-actin network spreads all over the cell, pushing the walls and causing friction on a large surface. For intermediate widths, the sides of the cell contact with a smaller area, which combined with a wider front, results in faster polymerization [24], and thus, faster motion. Comparing with F-actin distributions in experiments [Fig. 4(b), bottom] we can see how the F-actin network is in contact with both walls of the channel and is widespread across the cell, resulting in a characteristic rectangular shape [37]. However, our model is unable to reproduce some detailed dynamics experimentally observed in [24, 37], e.g., the presence of two kinds of F-actin networks. One of them, called *free* network, produces protrusions at the leading edge in a highly dynamic fashion. The other one is a denser network that polymerizes perpendicular to the channel wall, remains stationary with respect to the wall,
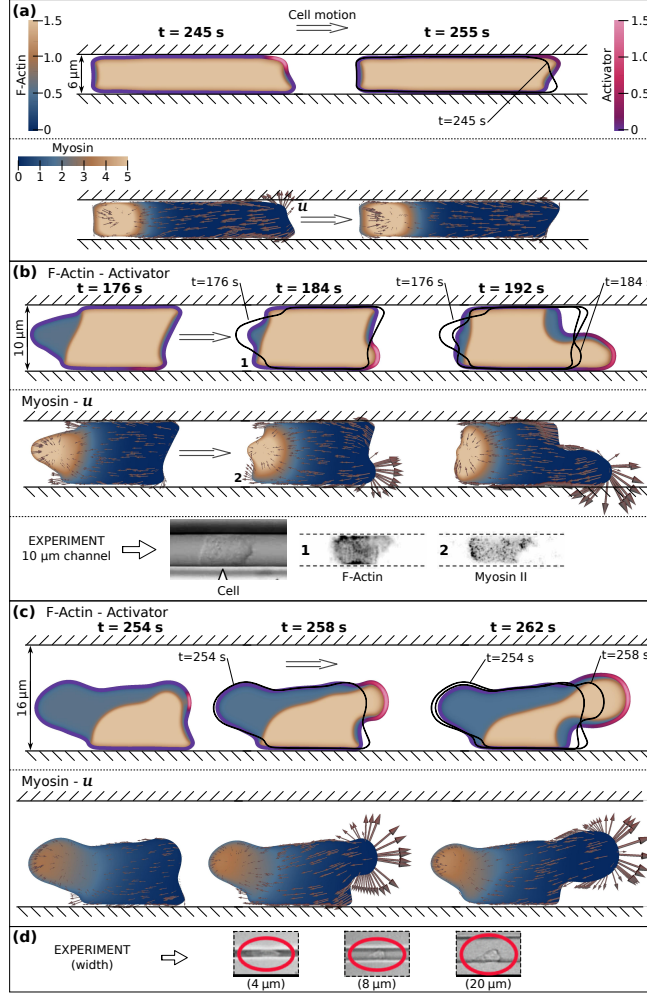
FIG. 4. (Color online) Cell motility in microchannels. F-actin and activator distributions (top of each panel), and myosin and velocity distributions (bottom of each panel) at different times. (a) 6 μm width channel at $t = 245$ and 255 s. (b) 10 μm width channel at $t = 176$, 184, and 192 s. At the bottom: cell shape, F-actin, and myosin experimental images in a 10 μm width channel, taken from [37]. (c) 16 μm width channel at $t = 254$, 258, and 262 s. (d) Experimental images for different widths, taken from [36].

and is called *adherent* network. As shown in Fig. 4(b), our model represents just one type of dense F-actin network: both the free and the adherent networks are associated to $\rho_f = 1.5$. To distinguish the two networks, we should modify the functional $\mathcal{F}$ [see Eq. (4)] to include another stable F-actin density that accounts for the adherent network. In addition, [24, 37] suggest that confinement produces a mechanical interaction between the actin networks. We have modeled the cell-wall contact through the membrane-located force $\boldsymbol{F}_{wall}$, but we
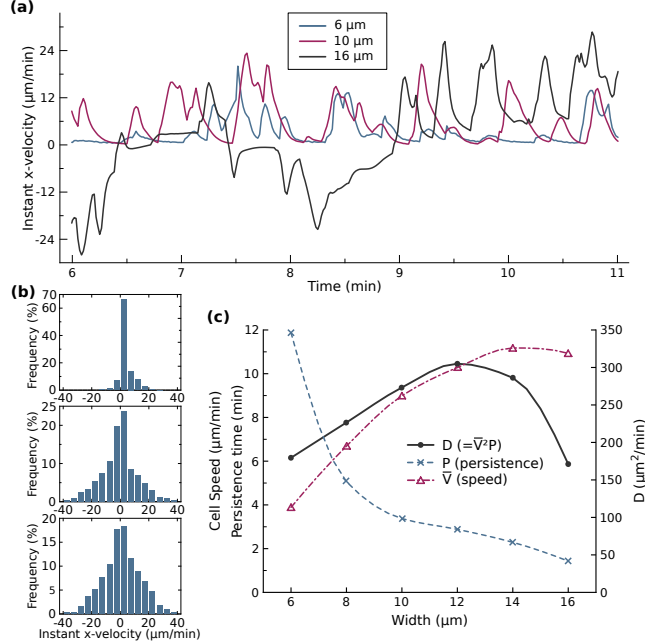
13

FIG. 5. (Color online) Results analysis of cell motility in microchannels. (a) Temporal evolution of instant x-velocity (in the channel's direction) for 6, 10, and 16 μm width channels. (b) Histograms of instant x-velocity for 6 (top subpanel), 10 (mid subpanel), and 16 μm (bottom subpanel) width channels. (c) Cell speed, persistence time, and parameter D, depending on channel width.

have not incorporated the feedback between confinement and actin dynamics, which could lead to a stationary adherent network. Finally, [37] describes an alternating zigzag motion at the cell front, while the back advances synchronously. This behavior is predicted by our model, mainly caused by the pseudopod extension probability [see Fig. 1(d)], which is annihilated in regions where the membrane is touching the wall. This constraint is also set in the activator-inhibitor system of [37], whose activator outcome displays similarities with the dynamics of our activator. A mild alternating motion as well as qualitatively realistic distributions of F-actin and myosin can be observed in the video included in [34].

We have measured the instant velocity and the persistence time for the different widths. Figure 5 shows how the speed increases as the channel becomes wider, reaching a maximum value that is close to the free-motion velocity. The persistence time decreases as the width increases, showing an obvious trend to random free motion for wider channels. These two features of confined movement can be observed in Fig. 5(a): for wide channels, the instant velocity reaches greater values, and the x-velocity (in the channel's direction) sign changes

14

more frequently, which means a decrease in the persistence time. The same conclusion can be drawn from Fig. 5(b) (note that initial conditions in the simulations imply x-velocity>0); the wider the channel is, the more symmetric the x-velocity histogram will be. The average velocity $(\bar{V})$ and the persistence time (P) for the different widths have been plotted in Fig. 5(c). Here, the parameter $D = \bar{V}^2 P$ is known to measure the cells ability to spread and disseminate [6, 38] (see Appendix A). It may be observed how D reaches a maximum for a channel width of $\sim 12\,\mu$m. This suggests that cells may exploit the geometry of their microenvironment to find effective migration strategies.

V. CONCLUSION

In conclusion, our results suggest that coupling intracellular and membrane dynamics is crucial to understand amoeboid motion. By including the main cytosolic compounds involved in cell motion, we are able to represent the dynamics inside the cell when amoeboid motility is taking place. The use of the phase-field method permits a simple treatment of phase transformations, avoids the use of moving meshes, which is especially important to model membrane dynamics, and simplifies the numerics. The model shows quantitative agreement with experiments of free and confined amoeboid motion. We believe that our model opens new opportunities to study also mesenchymal and chemotactic migration. The model can be extended in several ways. For example, replacing rigid obstacles with flexible fibers may provide insights to understand cell motion in the extracellular matrix.

Appendix A

1. Initial Conditions and Parameters used in the Simulations

The parameter values used in the simulations are shown in Table I. Some of them have been taken from the literature, representing experimental values. Others, which are introduced by the model, have been estimated.

In the case of free movement, we start with a circular cell or radius $8\,\mu\mathrm{m}$, and uniform distributions for the different fields: $\rho_m = 1.05\,\mu\mathrm{m}^{-2}$, $a = 0.0\,\mu\mathrm{m}^{-2}$, $\rho_f = 0.51\,\mu\mathrm{m}^{-2}$, $\rho_g = 1.1\,\mu\mathrm{m}^{-2}$, and $\boldsymbol{u} = 0.0\,\mu\mathrm{m\,s}^{-1}$. Note that the total amount of actin $\mathcal{N}_0$ and the total amount of myosin $\int_\Omega \phi\rho_m\,d\Omega$ are kept constant throughout the simulations. Since we need the location of the two previous pseudopods to define the probability distribution that provides $\delta_{\boldsymbol{x},i}$ [Fig. 1(d)], at the initial time we give two random locations for these points.

In the case of microchannel simulations, we start with a rectangular cell, adjusted to the channel width, with a suitable length so as to keep a physiological area. The initial distribution of activator and the initial velocity vanish again. The fields ρ_m, ρ_f, and ρ_g are initialized using different (uniform) values depending on the channel width, such that $\mathcal{N}_0$ and $\int_\Omega \phi\rho_m\,d\Omega$ are kept constant for all widths. In particular, we have adjusted the initial values of ρ_m and ρ_f to get $\mathcal{N}_0 = 430$ and $\int_\Omega \phi\rho_m\,d\Omega = 250$, by setting $\rho_g = 1.1\,\mu\mathrm{m}^{-2}$ at the beginning of the simulation.

2. Governing Equations

Throughout this work, we have employed markers to localize the membrane, the channel wall, and the activator sources, among others. These markers are defined using a smoothed out Heaviside function that we call $\mathcal{H}$. The function $\mathcal{H}$ is a hyperbolic tangent approximation of the actual Heaviside function H, which is defined as

$$H(x) = \begin{cases} 0, & x \leq 0 \\ 1, & x > 0 \end{cases} \tag{A1}$$

We employ the smooth function $\mathcal{H}$ rather than H in our model to improve the performance of our numerical algorithms.

TABLE I. Parameters used in the Simulations

Symbol	Description	Value	Data source
Γ	Lagrange multiplier	$0.52\,\mu\mathrm{m\,s^{-1}}$	[a][15]
ε	Phase-field interfacial length scale	$2\,\mu\mathrm{m}$	[15]
$D_{\max}$	Myosin diffusion scale	$4.16\,\mu\mathrm{m^2 s^{-1}}$	[a][39]
K	Decay rate of mysosin diffusion	$1.55\,\mu\mathrm{m^2}$	Estimated
D_a	Diffusion coefficient of activator	$0.195\,\mu\mathrm{m^2 s^{-1}}$	Estimated
r_a	Decay rate of activator	$0.325\ \mathrm{s^{-1}}$	Estimated
b_a	Production rate of activator	$7.8\ \mathrm{s^{-1}}$	Estimated
φ	Scaling of membrane marker width	25	[40]
a_{max}	Saturation of activator	$1.4\,\mu\mathrm{m^{-2}}$	Estimated
r_p	Radius of activator source	$1\,\mu\mathrm{m}$	Estimated
ε_f	Diffusive length scale of F-actin	$0.707\,\mu\mathrm{m}$	Estimated
ε_g	Diffusive length scale of G-actin	$3.16\,\mu\mathrm{m}$	Estimated
α	Penalty parameter for actin conservation	$0.06\,\mu\mathrm{m^{-2}}$	[40]
Γ_f	F-actin mobility	$0.52\ \mathrm{s^{-1}}$	Estimated
Γ_g	G-actin mobility	$0.52\ \mathrm{s^{-1}}$	Estimated
μ	Dynamic viscosity coefficient	$1500\ \mathrm{pN\,s\,\mu m^{-1}}$	[41]
λ	Bulk viscosity coefficient	$-500\ \mathrm{pN\,s\,\mu m^{-1}}$	[41]
$\bar{\eta}_m$	Strength of contractile forces	$22.1\ \mathrm{pN\,\mu m}$	[a][18]
A	Range of contractile forces	0.4117	Estimated
$\bar{\eta}_f$	Strength of protrusive forces	$1.22\cdot10^4\ \mathrm{pN\,\mu m^3}$	Estimated
B	Range of protrusive forces	0.07659	Estimated
ς	Substrate friction coefficient	$0.7\ \mathrm{pN\,s\,\mu m^{-3}}$	[a][39]
γ	Surface tension coefficient	$78\ \mathrm{pN}$	[42]
η_{rep}	Strength of repulsive forces	$4550\ \mathrm{pN\,\mu m}$	Estimated
ς_{fr}^M	Friction coefficient	$0.895\ \mathrm{pN\,\mu m^{-2}}$	Estimated
K_u	Scaling of frictional cell speed	$30\ \mathrm{s\,\mu m^{-1}}$	Estimated
ΔT_i	Growth time of pseudopods	See Fig. 1(d)	[5]
Δt_i	Time interval between pseudopods	See Fig. 1(d)	[5]

[a] Order-of-magnitude from

The spatial localizers of the activator source $\delta_{\boldsymbol{x},i}$ are defined as $\delta_{\boldsymbol{x},i} = \mathcal{H}(r_p - d_i(\boldsymbol{x}))$, where d_i represents the distance to the center of the activator source i and r_p its approximate radius. The center of the new activator source is given by a random variable defined by a probability distribution similar to that shown in Fig. 1(d), right. In the plot, the bar's length is proportional to the probability of pseudopod extension per unit length of cell's perimeter. This probability distribution depends on the location of the two previous sources (each source moves together with the membrane) as we have explained in the main text. Therefore, this probability function changes over time. Note that the cell-obstacle contact impedes pseudopod formation [37], thus modifying the probability distribution $[P_{PE}(\boldsymbol{x}) = 0$ if $d(\boldsymbol{x}) < 1.3$, where $d(\boldsymbol{x})$ is the distance from point $\boldsymbol{x}$ to the closest obstacle].

To define the temporal localizers of the function S_a [see Eq. (3) in the main text], we consider a set of times $\{t_{0,1}, t_{0,2}, \dots\}$, such that $t_{0,i}$ is the time at which the activator source that creates pseudopod i is switched on. We take $t_{0,1} = 0$ and $t_{0,i} = t_{0,i-1} + \Delta t_i$, where Δt_i is called *interval*, and represents the time interval between the extension of two consecutive pseudopods. The interval is a random variable whose distribution is given on the top middle of Fig. 1(d). Finally, the temporal localizers can be defined as $\delta_{t,i} = \mathcal{H}(\Delta T_i - (t - t_{0,i}))$, where ΔT_i is the growth time of pseudopod i, which is another random variable with the distribution shown in the top left plot of Fig. 1(d).

In summary, each time a new pseudopod emerges, we need to pick three values corresponding to the previous distributions: one corresponds to the location of the center of the activator source, another represents the time during which the source will be active (ΔT_i), and the remaining one defines the time at which the next pseudopod will arise (Δt_i). Note that the probability distributions plotted in Fig. 1(d) are precise approximations of statistical experimental data taken from [5].

To achieve accurate results using Eq. (3) we need to employ a steep marker δ_m [20], as well as a fine computational mesh. The need for a very steep marker δ_m and a very fine mesh may be by-passed by replacing $\boldsymbol{u}$ with $\boldsymbol{u}^\star$ in Eq. (3). The field $\boldsymbol{u}^\star$ is obtained by defining a constant extension of the velocity $\boldsymbol{u}$ at the level set $\phi = 0.5$ in the direction orthogonal to the membrane, that can be approximated by $\boldsymbol{u}^\star(\boldsymbol{x}) = \boldsymbol{u}(\boldsymbol{x}_A)$, where $\boldsymbol{x}_A$ is the closest point to $\boldsymbol{x}$ such that $\phi(\boldsymbol{x}_A) = 0.5$. We found that this procedure significantly speeds up the computations, introducing negligible errors.

The functions $\eta_m(\rho_m)$ and $\eta_f(\rho_f)$ controlling the contractile and protrusive stresses in

Eq. (10) are expressed as

$$\eta_m(\rho_m) = A\bar{\eta}_m + (1 - A)\bar{\eta}_m\mathcal{H}(\rho_m - 0.9), \tag{A2}$$

$$\eta_f(\rho_f) = B\bar{\eta}_f + (1 - B)\bar{\eta}_f\mathcal{H}(\rho_f - 1.0), \tag{A3}$$

where A, B, $\bar{\eta}_m$ and $\bar{\eta}_f$ are constants.

The markers employed in Eq. (10) can be expressed as

$$\delta_f = \mathcal{H}(d(\boldsymbol{x}) - 1.6) \tag{A4}$$

$$\delta_{wall}^{rep} = \mathcal{H}(0.7 - d^\star(\boldsymbol{x})) \tag{A5}$$

$$\delta_{fr} = \delta_{mem}\delta_{wall}^{fr}\delta_p \tag{A6}$$

$$\delta_{mem} = \mathcal{H}(0.45 - |\phi - 1/2|) \tag{A7}$$

$$\delta_{wall}^{fr} = \mathcal{H}(1.0 - d^\star(\boldsymbol{x})) \tag{A8}$$

$$\delta_p = \mathcal{H}(\rho_f - 1.0) \tag{A9}$$

where $d(\boldsymbol{x})$ is the distance from point $\boldsymbol{x}$ to the closest obstacle. To determine $d^\star(\boldsymbol{x})$, we make use of the same idea employed for $\boldsymbol{u}^\star$, i.e., $d^\star(\boldsymbol{x}) = d(\boldsymbol{x}_A)$. The field $d^\star$ only plays a role in a small neighborhood of the membrane and represents the net distance between the obstacle and the membrane. For example, δ_{wall}^{rep} is active ($\delta_{wall}^{rep} \sim 1$) when the distance of the membrane to the wall is lower than $0.7\,\mu\mathrm{m}$. The marker δ_{fr} corresponds to the friction force, which arises in the cell membrane (defined by δ_{mem}) when a pseudopod (marked by δ_p in the model) is pushing the wall (δ_{wall}^{fr}).

3. Mean Squared Displacement and Diffusion Coefficient D

The *mean squared displacement*, defined as $\mathrm{MSD}(t) = (\sum_{i=1}^{n_c} |\boldsymbol{x}_i(t) - \boldsymbol{x}_i(0)|^2)/n_c$, where n_c is the number of cells and $\boldsymbol{x}_i(t)$ is the position of the cell's centroid at time t, is a common measure of the spatial extent of random motion. For persistent random motion, the MSD can be fitted by $\mathrm{MSD}(t) = 2n_d D[t - P(1 - \exp(-t/P))]$, where n_d is the number of dimensions, P is the persistence time, and D is the augmented diffusion constant [6]. D is the parameter controlling the ability of cells to spread and disseminate that we use for the quantitative study of migration in microchannels in the main text. If we perform the velocity autocovariance analysis [6], applied to the general case of n_d dimensions, we get

$$D = \frac{\bar{V}^2 P}{n_d}, \tag{A10}$$

where $\bar{V}$ is the average cell speed.

For free planar movement, $n_d = 2$ [this case corresponds to Fig. 3(b), where our data can be adjusted to the previous formula $\text{MSD}(t)$, resulting $D = 233.3\,\mu\text{m}^2/\text{min}$]. However, for confined motility inside channels, the movement of the cells is restricted by the walls. If the width of the microchannel is small enough, we can consider that there is only one direction of dispersal, and we can take $n_d = 1$. Therefore, in Fig. 5(c), P and $\bar{V}$ are obtained directly from our simulations, and the diffusion coefficient D is calculated using Eq. (A10), with $n_d = 1$.

---

[1] E. T. Roussos, J. S. Condeelis, and A. Patsialou, Nat. Rev. Cancer **11**, 573 (2011).

[2] P. Friedl and D. Gilmour, Nat. Rev. Mol. Cell Biol. **10**, 445 (2009).

[3] P. Friedl and K. Wolf, Nat. Rev. Cancer **3**, 362 (2003).

[4] R. H. Insall, Nat. Rev. Mol. Cell Biol. **11**, 453 (2010).

[5] L. Bosgraaf and P. J. M. Van Haastert, PLoS ONE **4**, e5253 (2009).

[6] M. J. Potel and S. A. Mackay, J. Cell Sci. **36**, 281 (1979).

[7] M. H. Gail and C. W. Boone, Biophys. J. **10**, 980 (1970).

[8] A. Jilkine and L. Edelstein-Keshet, PLoS Comput. Biol. **7**, e1001121 (2011).

[9] W. R. Holmes and L. Edelstein-Keshet, PLoS Comput. Biol. **8**, e1002793 (2012).

[10] H. Meinhardt, J. Cell Sci. **112**, 2867 (1999).

[11] A. Levchenko and P. A. Iglesias, Biophys. J. **82**, 50 (2002).

[12] C. M. Elliott, B. Stinner, and C. Venkataraman, J. R. Soc. Interface **9**, 3027 (2012).

[13] I. Hecht, M. L. Skoge, P. G. Charest, E. Ben-Jacob, R. A. Firtel, W. F. Loomis, H. Levine, and W.-J. Rappel, PLoS Comput. Biol. **7**, e1002044 (2011).

[14] D. Shao, W.-J. Rappel, and H. Levine, Phys. Rev. Lett. **105**, 108104 (2010).

[15] D. Shao, H. Levine, and W.-J. Rappel, Proc. Natl. Acad. Sci. U.S.A. **109**, 6851 (2012).

[16] A. Dreher, I. S. Aranson, and K. Kruse, New J. Phys. **16**, 055007 (2014).

[17] G. Danuser, J. Allard, and A. Mogilner, Annu. Rev. Cell Dev. Biol. **29**, 501 (2013).

[18] B. Rubinstein, M. F. Fournier, K. Jacobson, A. B. Verkhovsky, and A. Mogilner, Biophys. J. **97**, 1853 (2009).

[19] T. Biben, K. Kassner, and C. Misbah, Phys. Rev. E **72**, 041921 (2005).

[20] K. E. Teigen, X. Li, J. Lowengrub, F. Wang, and A. Voigt, Commun. Math. Sci. **4**, 1009 (2009).

[21] P. J. M. Van Haastert and P. N. Devreotes, Nat. Rev. Mol. Cell Biol. **5**, 626 (2004).

[22] H. Emmerich, *The diffuse interface approach in materials science: thermodynamic concepts and applications of phase-field models*, Vol. 73 (Springer Science & Business Media, 2003).

[23] Numerical simulations introducing bending forces with realistic values of the bending stiffness have been performed and do not alter the results.

[24] K. Wilson, A. Lewalle, M. Fritzsche, R. Thorogate, T. Duke, and G. Charras, Nat. Commun. **4**, 2896 (2013).

[25] R. J. Hawkins and R. Voituriez, Math. Model. Nat. Phenom. **5**, 84 (2010).

[26] S. Gabriele, A.-M. Benoliel, P. Bongrand, and O. Theodoly, Biophys. J. **96**, 4308 (2009).

[27] P. Preira, M.-P. Valignat, J. Bico, and O. Theodoly, Biomicrofluidics **7**, 024111 (2013).

[28] F. Gerbal, P. Chaikin, Y. Rabin, and J. Prost, Biophys. J. **79**, 2259 (2000).

[29] Y. Mori, A. Jilkine, and L. Edelstein-Keshet, Biophys. J. **94**, 3684 (2008).

[30] M. P. Neilson, D. M. Veltman, P. J. M. Van Haastert, S. D. Webb, J. A. Mackenzie, and R. H. Insall, PLoS Biol. **9**, e1000618 (2011).

[31] J. Zhang, S. Das, and Q. Du, J. Comput. Phys. **228**, 7837 (2009).

[32] I. Hecht, H. Levine, W.-J. Rappel, and E. Ben-Jacob, PLoS ONE **6**, e21955 (2011).

[33] T. J. R. Hughes, J. A. Cottrell, and Y. Bazilevs, Comput. Methods in Appl. Mech. Eng. **194**, 4135 (2005).

[34] See Supplemental Material at [URL will be inserted by publisher] with videos of the simulations.

[35] L. Li, S. F. Nørrelykke, and E. C. Cox, PLoS ONE **3**, e2093 (2008).

[36] J. Jacobelli, R. S. Friedman, M. A. Conti, A. M. Lennon-Dumenil, M. Piel, C. M. Sorensen, R. S. Adelstein, and M. F. Krummel, Nat. Immunol. **11**, 953 (2010).

[37] O. Nagel, C. Guven, M. Theves, M. Driscoll, W. Losert, and C. Beta, PLoS ONE **9**, e113382 (2014).

[38] G. E. Uhlenbeck and L. S. Ornstein, Phys. Rev. **36**, 823 (1930).

[39] B. A. Camley, Y. Zhao, B. Li, H. Levine, and W.-J. Rappel, Phys. Rev. Lett. **111**, 158102 (2013).

[40] Parameters of the computational algorithm.

[41] A. R. Bausch, F. Ziemann, A. A. Boulbitch, K. Jacobson, and E. Sackmann, Biophys. J. **75**, 2038 (1998).

[42] J. Y. Tinevez, U. Schulze, G. Salbreux, J. Roensche, J. F. Joanny, and E. Paluch, Proc. Natl. Acad. Sci. U.S.A. **106**, 18581 (2009).